Received: 6 July 2021 | Revised: 30 August 2021 | Accepted: 30 August 2021

DOI: 10.1111/jace.18120

Journal of the American Ceramic Society

RESEARCH ARTICLE

Variable thermochemical stability of $RE_2Si_2O_7$ (RE = Sc, Nd, Er, Yb, or Lu) in high-temperature high-velocity steam

Mackenzie Ridley | **Elizabeth Opila**

Materials Science and Engineering, University of Virginia, Charlottesville, Virginia, USA

Correspondence
Mackenzie Ridley, Materials Science and Engineering, University of Virginia, Charlottesville, Virginia, USA.
Email: mjr3be@virginia.edu

Funding information
National Science Foundation DMREF: Collaborative Research: GOALI: Accelerating Discovery of High Entropy Silicates for Extreme Environments, Grant/Award Number: #1921973

Abstract

Five rare-earth (RE) disilicates ($RE_2Si_2O_7$, RE = Sc, Nd, Er, Yb, or Lu) were synthesized and exposed to high-velocity steam (up to 235 m/s) for 125 hours at 1400°C. Water vapor reaction products, mass loss, average reaction depths, and product phase microstructural evolution were analyzed for each material after exposure. Similar to steam testing results in the literature, $RE_2Si_2O_7$ (RE = Er, Yb, Lu) underwent silica depletion producing gaseous silicon hydroxide species, RE_2SiO_5, and RE_2O_3 product phases. $Sc_2Si_2O_7$ reacted with high-velocity steam to produce only a Sc_2O_3 product layer with no stable Sc_2SiO_5 phase detected by X-ray diffraction or microscopy techniques. Further, $Nd_2Si_2O_7$ rapidly reacted with steam to produce $Nd_{9.33}\square_{0.67}Si_6O_{26}$ with no Nd_2SiO_5 or Nd_2O_3 reaction products. All $RE_2Si_2O_7$ that produced a silicate reaction product (RE = Nd, Er, Yb, Lu) showed densification of the product phase at steam velocities above 150 m/s that resulted in enhanced resistance. The results presented in this work demonstrate that rare-earth silicates show diverse steam reaction products, reaction product microstructures, and total reaction depths after high-temperature high-velocity steam exposure. Of the materials in this study, $RE_2Si_2O_7$ (RE = Yb, Lu) were most stable in high-temperature high-velocity steam, making them most desirable as environmental barrier coating candidates.

KEYWORDS
degradation, environmental barrier coatings (EBC), microstructure, rare earths, silicates

1 | INTRODUCTION

Environmental barrier coatings (EBCs) are required for the protection of high-temperature structural ceramics, such as SiC, in gas-turbine applications. EBCs must protect their underlying substrate by limiting substrate and silicon bond coat oxidation, steam degradation, and molten CaO-MgO-Al_2O_3-SiO_2 (CMAS) attack over extended time periods and thermal cycles. Therefore, EBC candidates must possess a high melting temperature, minimal thermal expansion mismatch with SiC, chemical stability with SiC, and chemical resistance to both steam (gas turbine combustion byproduct) and CMAS (ingested debris). Rare-earth (RE) disilicates, $RE_2Si_2O_7$, represent the current standard for EBC materials. The relative steam reactivity of rare-earth silicates remains not well understood due to the variety of experimental facilities used to test these materials.

SiC, a composite structural material for lightweight turbine components, is known to form a silica (SiO_2) thermally grown oxide after exposure to oxygen at elevated temperatures (Equation 1). The oxide scale reacts with steam from combustion environments to produce a silicon

hydroxide ($Si(OH)_4$ (g)) gas species (Equation 2) that inevitably result in component degradation[1]:

$$SiC + \frac{3}{2} O_2\,(g) \rightarrow SiO_2 + CO\,(g), \quad (1)$$

$$SiO_2 + 2H_2O\,(g) \rightarrow Si(OH)_4\,(g). \quad (2)$$

$RE_2Si_2O_7$ are silicate ceramics, and thus also react with steam to form $Si(OH)_4$ (g), although at a reduced rate compared to pure SiO_2 due to a decreased silica activity. It has been assumed that all $RE_2Si_2O_7$ behave similarly in steam environments through the production of a $Si(OH)_4$ (g) species as shown in Equation (3).

$$RE_2Si_2O_7 + 2H_2O\,(g) \rightarrow RE_2SiO_5 + Si(OH)_4\,(g) + \text{porosity}. \quad (3)$$

The silica activity for the RE_2SiO_5-$RE_2Si_2O_7$ (RE = Y, Yb, and Lu) dual-phase field has been calculated to be near 0.3 at 1500°C.[2–4] The disilicates in these Y, Yb, and Lu silicate systems are all the monoclinic β-phase $RE_2Si_2O_7$ polymorph, which implies that rare-earth disilicates with the same polymorph and similar rare-earth cation size will have comparable silica activities. The silica activities for other $RE_2Si_2O_7$ polymorphs have not yet been determined.

1.1 | $RE_2Si_2O_7$

RE = Sc, Er, Yb, and Lu disilicates all are monoclinic with space group C2/m, termed β-phase disilicates,[5] at the temperatures of interest in this work. This phase is the desired phase for EBC candidates due to the associated low coefficient of thermal expansion (CTE) in the range of 3.9–5.4 × 10^{-6}/°C.[6] $Nd_2Si_2O_7$ is a tetragonal P41 space group, often termed A-phase, and has a much higher linear thermal expansion of 10.5 × 10^{-6}/°C.[7] Due to the thermal expansion mismatch, $Nd_2Si_2O_7$ is therefore not a desirable standalone EBC coating material on SiC, which has a CTE of 4.5–5.5 × 10^{-6}/°C.[8] Both RE = Er and Nd also have a polymorph transition in the temperature range of turbine applications, which would make them unsuitable as EBC candidates without stabilizing a single phase up to 1600°C. Phase stabilization has been shown in the literature, where the high-temperature polymorphs for $Y_2Si_2O_7$ and $Er_2Si_2O_7$ were avoided through stabilization of the β-phase via mixing of multiple rare-earth cations in solid solution.[9,10]

The Yb_2O_3-SiO_2[11], Sc_2O_3-SiO_2[12], and Nd_2O_3-SiO_2[13] pseudobinary phase diagrams have been overlaid in Figure 1. The Yb_2O_3-SiO_2 diagram is representative of RE = Er or Lu phase diagrams in terms of stable line compounds.

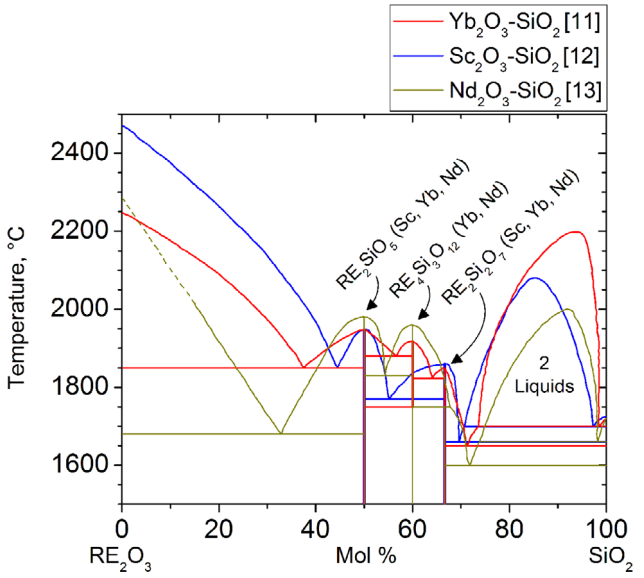

FIGURE 1 Overlaid pseudobinary phase diagrams of the Yb_2O_3-SiO_2,[11] Sc_2O_3-SiO_2,[12] and Nd_2O_3-SiO_2[13] systems

Stable line compounds include SiO_2, $RE_2Si_2O_7$, $RE_4Si_3O_{12}$, RE_2SiO_5, and RE_2O_3. For RE = Er, Yb, and Lu systems, the intermediate rare earth apatite phase ($RE_4Si_3O_{12}$) is only stable at high temperatures (1750–1920°C for RE = Yb) outside the range of interest so that the disilicate and monosilicate line compounds are the only stable phases of interest. The intermediate apatite line compound ($Sc_4Si_3O_{12}$) is not present for the Sc_2O_3-SiO_2 system. The Nd_2O_3-SiO_2 system shows greater stability of the apatite phase, with variability in the stable temperature region and composition reported in the literature. The Nd_2O_3-SiO_2 phase diagram by Toropov displays the $Nd_4Si_3O_{12}$ apatite line compound with predicted stability to temperatures as low as 1500°C.[13] Toropov and Kougiya later showed that the $Nd_4Si_3O_{12}$ apatite phase was not a line compound but instead was a stable phase across ~7 mol % Nd_2O_3 at 1400°C.[14] The apatite phase composition has also been represented experimentally as $Nd_{9.33} \leq {}_{0.67}Si_6O_{26}$, a cation deficient apatite structure.[15] More recent computational modeling has also predicted that the apatite phase is better represented by $Nd_{9.33}\square_{0.67}Si_6O_{26}$ than $Nd_4Si_3O_{12}$, where small fluctuations in the Nd concentration are accounted for through site vacancies.[16,17] The melting temperatures for the line compounds are presented in Table 1 for reference.

1.2 | Steam reactivity of $RE_2Si_2O_7$

Steam reactivity of silicate EBC materials occurs through silica depletion via the production of $Si(OH)_4$ (g). Steam testing described in the literature has often been limited

TABLE 1 Melting temperatures of line compounds in the RE_2O_3-SiO_2 pseudobinary phase diagrams

Melting temperatures (°C)				
Rare earth	**RE_2O_3**	**RE_2SiO_5**	**$RE_4Si_3O_{12}$**	**$RE_2Si_2O_7$**
Sc[12]	2472	1950	N/A	1860
Nd[13]	2284	1980	1960	1750
Er[18]	2282	1980	1900	1800
Yb[11]	2250	1950	1920	1850
Lu[19]	2510	2000	1869	1860

to experimental setups with low steam velocities or low water vapor partial pressures, which do not approach the extreme environment of a gas turbine. As presented in Table 2 for steam testing described in the literature, near stagnant gas flow steam testing has often resulted in linear reaction kinetics, whereas high-velocity testing results in parabolic reaction kinetics.

$Yb_2Si_2O_7$ is one of the more extensively studied $RE_2Si_2O_7$ described in the literature due to its optimum thermal expansion match with SiC and acceptable high-temperature mechanical and chemical stability. Most literature states that $Yb_2Si_2O_7$ reacts with steam to form porous Yb_2SiO_5.[22–24] For high-velocity testing above 1200°C, parabolic reaction kinetics have been reported, which imply diffusion-controlled kinetics. Low steam velocity experimental setups often result in linear reaction kinetics and impurity uptake from furnace ware. The $Yb_2Si_2O_7$ data obtained at 1400°C from our laboratory are presented later in this work and have been described in detail elsewhere.[23] Ueno et al. have also extensively studied the $Lu_2Si_2O_7$ reaction in both low- and high-velocity steam. While SiO_2 at the starting grain boundaries limited steam reaction, Lu_2SiO_5 and trace Lu_2O_3 were observed after steam exposure.[26] It is assumed that $Lu_2Si_2O_7$ behaves similarly to $Yb_2Si_2O_7$ in terms of both steam resistance and steam reaction mechanism.

Only two studies of $Sc_2Si_2O_7$ steam resistance are found in the literature. Thermogravimetric analysis at near stagnant gas velocities showed non-linear mass loss with no reaction products, where mass loss can be attributed to excess SiO_2 volatility in steam.[20] Klemm et al. also reported burner rig testing of bulk $Sc_2Si_2O_7$ and Sc_2SiO_5 samples.[22] Their results indicated that $Sc_2Si_2O_7$ decomposed to Sc_2SiO_5 upon steam reaction and that Sc_2SiO_5 bulk samples decomposed to form Sc_2O_3 on the surfaces. All RE_2SiO_5 in their work were shown to be highly resistant to steam reaction. While the reaction products for $Sc_2Si_2O_7$ and Sc_2SiO_5 were found to be the same as those for RE = Yb and Lu, the stability of Sc silicates in steam environments was predicted to be less than that of other rare-earth silicates.[22]

Steam stability of rare-earth disilicates with a stable apatite compound in the temperature regions of EBC application, such as $Nd_2Si_2O_7$ in the Nd_2O_3-SiO_2 system, have not yet been reported in the literature. It is therefore unknown if the apatite phase will remain a stable product phase after the steam reaction. The authors have not found

TABLE 2 Steam testing of $RE_2Si_2O_7$ in the literature

Material	Temperature (°C)	Exposure time (h)	H_2O velocity (m/s)	P(H_2O) (atm)	P(Total) (atm)	Reaction products	Reaction kinetics	Notes
$Yb_2Si_2O_7$	1500	100	0.044	0.5	1	$Al_5Yb_3O_{12}$	Linear	Thermogravimetric analysis, excess Yb_2SiO_5 in starting material[20]
	1316	2000	0.044	0.9	1	Yb_2SiO_5	N/A	Steam cycling furnace, air plasma sprayed $Yb_2Si_2O_7$ on Si+SiC[21]
	1450	100–700	100	0.27	1	Yb_2SiO_5	Parabolic	Burner rig[22]
	1200, 1300, 1400	60, 125, 250	240	1	1	Yb_2SiO_5, Yb_2O_3	Parabolic	Steam jet[23]
$Lu_2Si_2O_7$	1300, 1500	100	50	Not provided	1	Lu_2SiO_5, $Lu_2Si_2O_7$	N/A	Excess SiO_2 in starting material[24]
	1500	310	0.13	0.3	1	$Al_5Lu_3O_{12}$	Not linear	$Al(OH)_3$ and $Si(OH)_4$ (g) saturation from furnace ware[25]
$Sc_2Si_2O_7$	1500	100	0.044	0.5	1	None	Linear	Thermogravimetric analysis, excess SiO_2 in starting material[20]
	1450	100–700	100	0.27	1	Sc_2SiO_5	Linear	Burner rig[22]

previous steam testing results for $Nd_2Si_2O_7$ or $Er_2Si_2O_7$ in the literature. Both the high-velocity steam reactivity and steam reaction products are not yet systematically investigated for all rare-earth silicate materials. This work compares $RE_2Si_2O_7$ (RE = Sc, Nd, Er, Yb, Lu) to verify steam stabilities and compare the microstructural evolution of steam reaction products.

2 | EXPERIMENTAL

2.1 | Processing

Samples were produced from high purity pre-reacted $RE_2Si_2O_7$ (Praxair). $RE_2Si_2O_7$ (RE = Sc, Er,, Lu) granules were annealed at 900°C for 30 min to bake off organics supporting the granules to result in sub-micron powder sizes, followed by ball milling with yttria-stabilized zirconia milling media for 24 h. Both $Nd_2Si_2O_7$ and $Yb_2Si_2O_7$ powders were ball-milled particulate as-received with a particulate size of ~1 μm and therefore were not heat-treated or ball-milled prior to processing. Powders were loaded into a 20-mm diameter graphite die and sintered in an argon atmosphere using spark plasma sintering (DCS 25-10 SPS, Thermal Technologies) at 65 MPa with maximum temperatures of 1560–1600°C for 30 min. The resulting pucks were then placed in an open-air box furnace (CM Rapid Furnace) for 24 h at 1400–1500°C to restore oxygen stoichiometry. All samples displayed relative densities ≥93%, determined from the Archimedes method. Sample coupons were sectioned from the annealed pucks to produce 10 × 10 × 1 mm coupons and polished to 0.25 μm with diamond suspension prior to characterization and steam exposure.

2.2 | Steam testing

Steam testing was performed in a modified Al_2O_3 tube furnace, termed a steam jet. More detailed information on the steam jet experimental setup can be found elsewhere.[27–29] Deionized water was pumped at 2 ml/min into a 1-mm inner diameter platinum/rhodium alloy capillary centered in a preheater at 900°C. As the liquid water vaporizes, the liquid-to-gas volume expansion leads to accelerated steam velocities exiting the capillary into the tube furnace. The sample is fixed on an Al_2O_3 support stand with platinum foil and wire at a 45° angle and a 1-mm distance relative to the capillary outlet in the center of the tube furnace hot zone. The proximity of the sample to the capillary outlet allows for high-velocity steam to impinge upon the sample surface with a water vapor partial pressure of 1 atm, thus preventing tube furnace impurities from reacting with most of the coupon face. The gas velocity across the coupons was calculated with ANSYS computational fluid dynamics (CFD) module (Canonsburg) to correlate local sample morphologies to steam velocities, ranging from near stagnant gas flow to a maximum of ~235 m/s at the sample impingement site as shown in Figure 2.

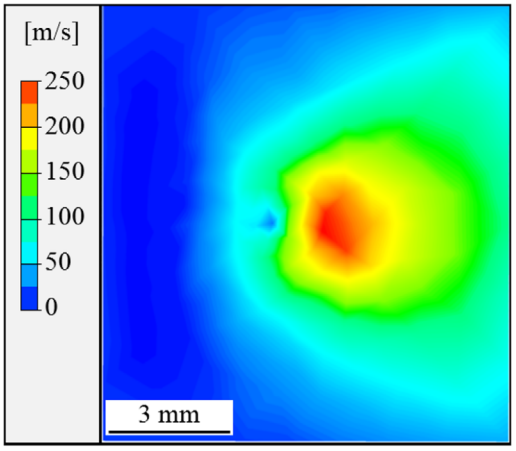

FIGURE 2 ANSYS steam velocity distribution across the sample face at 1400°C for a 2 ml/min water flow rate

Each $RE_2Si_2O_7$ coupon was exposed to steam at 1400°C for 125 h. Sample mass was recorded before and after exposure (MS105DU, Mettler-Toledo). X-ray diffraction (XRD, Panalytical Empyrean X-ray diffractometer) and scanning electron microscopy (SEM: FEI Quanta 650) with energy dispersive spectroscopy (EDS: Oxford Instruments) were used for analysis in plan view to determine surface reaction products. Coupons were then mounted in cross-section and polished through the center of the highest velocity impingement site for further SEM/EDS analysis to measure reaction depths and morphology changes. Pore formation and cross-section SEM images were analyzed in ImageJ Analysis Suite. Reaction depth measurements were taken around 70–110 μm apart across 2–7 mm cross-section distances, depending on the region of interest.

3 | RESULTS

3.1 | Initial $RE_2Si_2O_7$ characterization

Prior to steam testing, the sample purity, starting microstructure, and pore fraction were determined with both XRD and SEM/EDS. Backscattered electron SEM of the starting samples are presented in Figure 3, and the starting material properties are shown on Table 3. Both $Er_2Si_2O_7$ and $Nd_2Si_2O_7$ displayed sample cracking from high-temperature phase transformations near 1325 and 1410°C, respectively, resulting in decreased sample density compared to $RE_2Si_2O_7$ (RE = Sc, Yb, Lu).

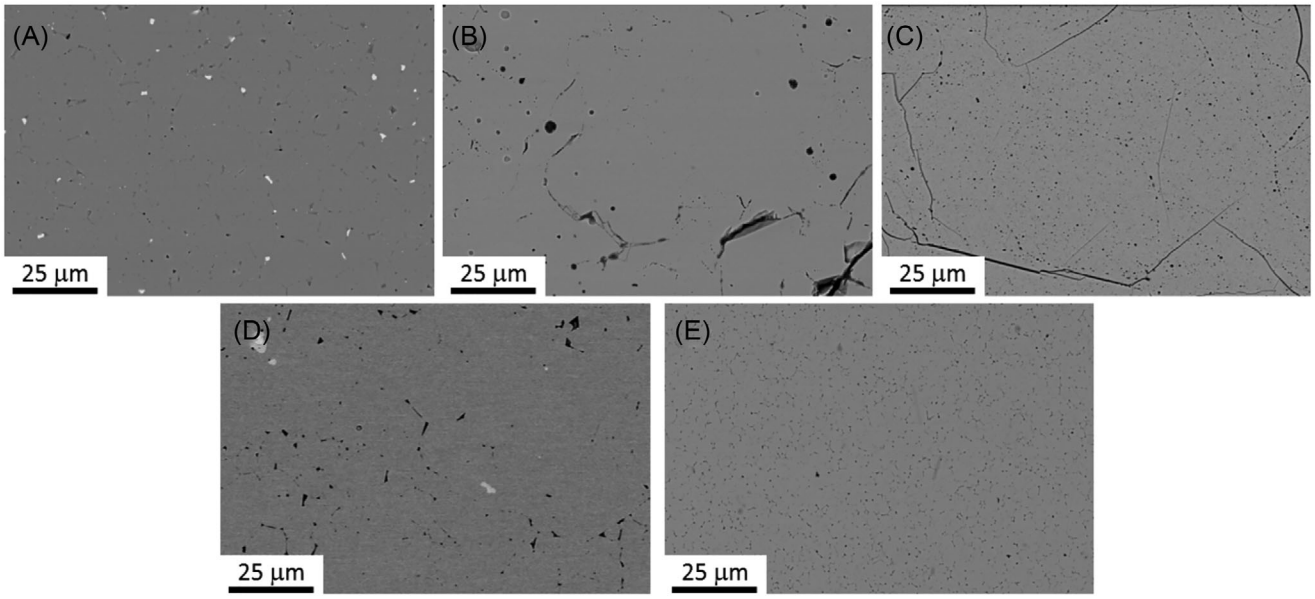

FIGURE 3 Starting microstructures of $RE_2Si_2O_7$. (A) $Sc_2Si_2O_7$, (B) $Nd_2Si_2O_7$, (C) $Er_2Si_2O_7$, (D) $Yb_2Si_2O_7$, and (E) $Lu_2Si_2O_7$

TABLE 3 Porosity Area Percent, secondary phases, crystal structure, and densities for the processed $RE_2Si_2O_7$

Sample	Porosity Area Percent	Minor phase fraction	Stable phase	Theoretical density (g/cm^3)	Archimedes (g/cm^3), % theoretical density
$Sc_2Si_2O_7$	2%	ZrO_2, 2%	β, C2/m	3.396[30]	3.31 ± 0.01, 98%
$Nd_2Si_2O_7$	10%	N/A	A, P41	5.45[31]	5.1 ± 0.1, 93%
$Er_2Si_2O_7$	6%	N/A	β, C2/m	6.099[32]	5.7 ± 0.2, 93%
$Yb_2Si_2O_7$	4%	Yb_2SiO_5, 2%	β, C2/m	5.151[33]	6.03 ± 0.03, 98%
$Lu_2Si_2O_7$	4%	N/A	β, C2/m	6.249[34]	6.10 ± 0.03, 98%

3.2 | $RE_2Si_2O_7$ (Re = Er, Yb, Lu)

Figure 4 displays XRD patterns for RE = Er, Yb, and Lu coupons before and after steam exposure at 1400°C for 125 h. For all three materials, the RE_2SiO_5 monosilicate phase is the predominant product species that forms upon steam reaction. Additionally, RE_2O_3 oxide patterns were matched to each scan, representing a secondary reaction product that is fully depleted of SiO_2. The $Yb_2Si_2O_7$ coupon additionally displayed $Yb_3Al_5O_{12}$ peaks that are representative of impurity deposition from $Al(OH)_3$ (g) resulting from reaction of the alumina furnace ware with H_2O (g). Alumina uptake was seen by SEM only at sample edges for all samples, yet XRD peaks for alumina uptake could not be identified on the RE = Er, Lu coupons. It will be shown that alumina impurity-containing phases are not forming in the regions of interest for analysis.

Plan view backscattered SEM imaging of $RE_2Si_2O_7$ (RE = Er, Yb, Lu) allows for visual analysis of various regions across the coupons where steam velocity and water vapor partial pressure can vary. Figure 5A displays the sample region underneath the platinum foil sample holder, where gas velocities are near stagnant. Initial RE_2SiO_5 formation in this region (light gray) forms along cracks and grain boundaries as a fairly dense surface layer on the $RE_2Si_2O_7$ base material (dark gray). No rare earth oxide formation is seen under the platinum foil . Figure 5B displays the RE_2SiO_5 product layer morphology at intermediate gas velocities of 80–115 m/s. RE = Er, Yb, and Lu coupons all display a fine porous structure where the product grain size is independent of the starting coupon grain size. At the highest velocities, shown in Figure 5C, RE_2O_3 formation is dominant on the surface. Gas velocities in this region are calculated to be 150–200 m/s. The oxide formation shows increased porosity formation, compared to the RE_2SiO_5 product layer in Figure 5B.

Figure 6 displays RE = Er, Yb, Lu coupon cross-sections so that the reaction depth can be analyzed. All three materials displayed similar behavior in steam. Figure 6A is representative of the 80–115 m/s velocity range shown

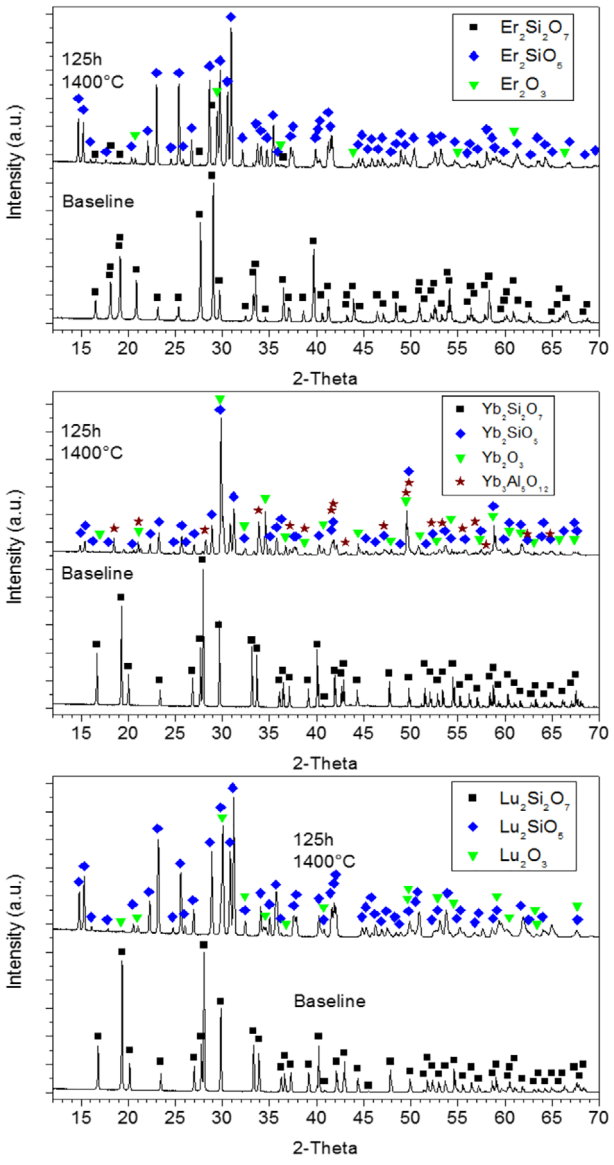

FIGURE 4 X-ray diffraction (XRD) of $RE_2Si_2O_7$ (RE = Er, Yb, and Lu) before and after steam exposure at 1400°C for 125 h

earlier in the plan view. Here, porous RE_2SiO_5 forms on the coupons, with porosity oriented perpendicular to the reaction interface. Increasing the gas velocity to 115–150 m/s, Figure 6B shows densification of the outer layer of the RE_2SiO_5 product phase. Densification of the product layer limits gas ingress to the reaction layer so that the total reaction depth decreased, compared to the intermediate gas velocity regime of 80–115 m/s. Finally, Figure 6C shows RE_2O_3 formation occurring on top of the densified RE_2SiO_5 layer with a continual decrease in total reaction thickness. Oxide formation implies that the dense RE_2SiO_5 layer is preventing steam reaction with the $RE_2Si_2O_7$ coupons. Therefore, oxide formation is occurring as a secondary reaction of the RE_2SiO_5 product phase.

3.3 | $Sc_2Si_2O_7$

$Sc_2Si_2O_7$ shows unique behavior, compared to the previous $RE_2Si_2O_7$ (RE = Er, Yb, Lu), in that Sc_2O_3 is the only product detected after steam exposure. XRD of $Sc_2Si_2O_7$ before and after steam exposure is shown in Figure 7. All peaks were matched to either the baseline $Sc_2Si_2O_7$ pattern or Sc_2O_3. The largest Sc_2O_3 peak (222 hkl plane) displayed a higher intensity, compared to the predicted peak heights for Sc_2O_3, representing the preferential orientation of the oxide after the steam reaction.

Plan view SEM images of $Sc_2Si_2O_7$ after steam exposure are shown in Figure 8. Figure 8A displays the highest velocity impingement site, where excess material loss attributed to mechanical erosion was recorded. Under the platinum foil at near-stagnant gas velocities (Figure 8B), Sc_2O_3 readily formed across the surface. No Sc_2SiO_5 formation was identified by SEM/EDS in this region even though the local environment was less extreme than at other regions across the sample face. Figure 8C is representative of the majority of the sample surface for all gas velocities 80–200 m/s. Here, sub-micron grain size Sc_2O_3 formation is present across the sample face with a high amount of sample porosity.

A representative backscattered SEM image of the reaction depth for $Sc_2Si_2O_7$ after steam exposure is shown in Figure 9A. Sc_2O_3 formation on $Sc_2Si_2O_7$ did not show notable velocity dependence across the majority of the sample, where gas velocities are calculated to be 80–200 m/s. The Sc_2O_3 morphology is additionally constant throughout the thickness of the reaction layer. Figure 9B displays sub-micron Sc_2O_3 particulate formed with orientation preference perpendicular to the reaction interface. An EDS line scan across the reaction interface in Figure 9C confirms that Sc_2SiO_5 is not forming at the reaction interface and that Sc_2O_3 is the dominant reaction product for the $Sc_2Si_2O_7$-steam reaction.

3.4 | $Nd_2Si_2O_7$

XRD results of the $Nd_2Si_2O_7$ surface before and after steam exposure for 124 h at 1400°C are shown in Figure 10. A-phase $Nd_2Si_2O_7$ readily reacted with steam to form an apatite phase, $Nd_{9.33}\square_{0.67}Si_6O_{26}$. While $Nd_4Si_3O_{12}$ ($2Nd_2O_3{\cdot}3SiO_2$) rather than $Nd_{9.33}\square_{0.67}Si_6O_{26}$ ($7Nd_2O_3{\cdot}9SiO_2$) is shown on the Nd_2O_3-SiO_2 phase diagram, $Nd_{9.33}\square_{0.67}Si_6O_{26}$ is extensively reported in the XRD database and in the literature as the stable Nd silicate cation deficient apatite phase.[35,36] Preferential orientation of the (n00) n = 1–6 hkl planes was observed for the $Nd_{9.33}\square_{0.67}Si_6O_{26}$ phase, with relative peak intensities 2.5–3.3 times greater than the reference pattern.

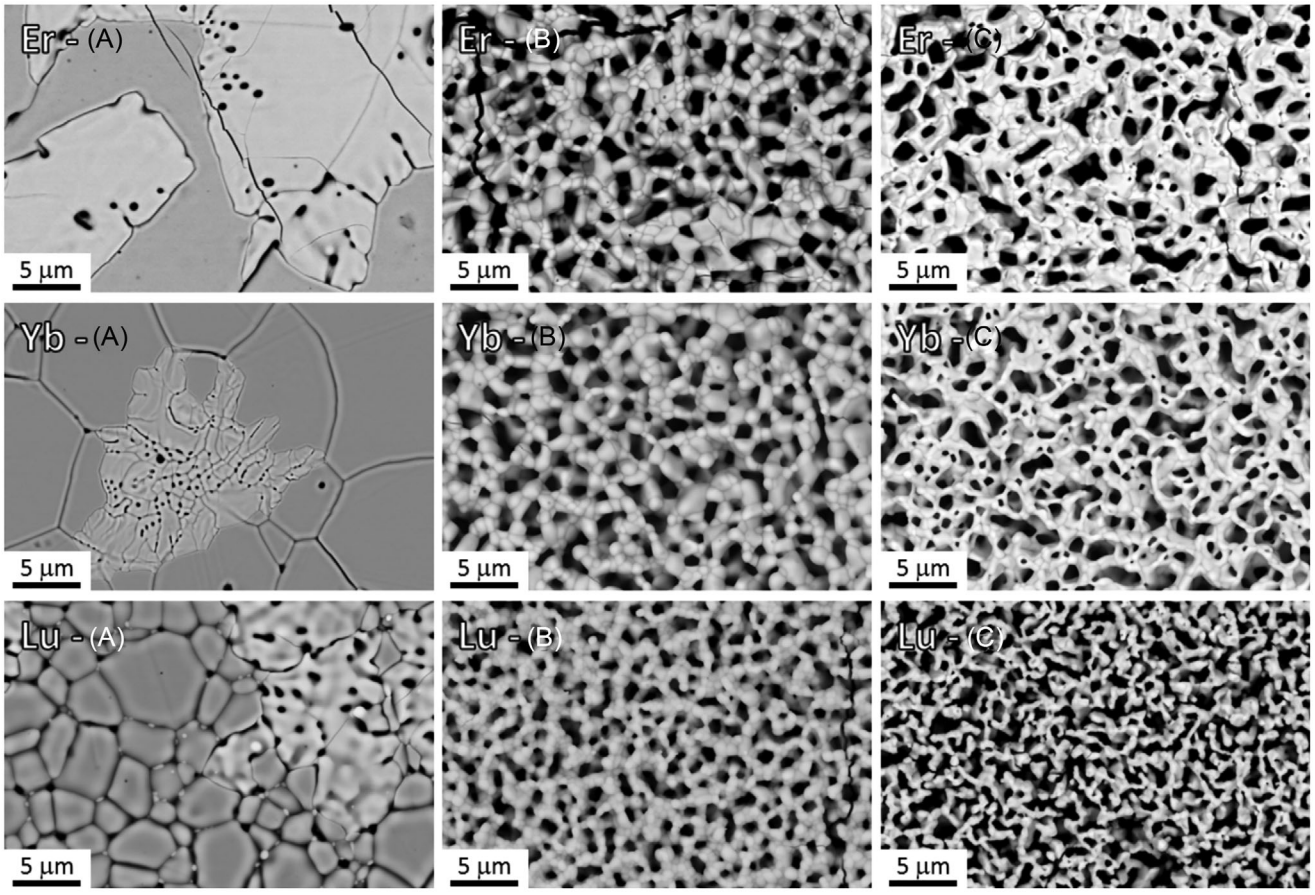

FIGURE 5 Representative backscattered electron scanning electron microscopy (SEM) images of $RE_2Si_2O_7$ (RE = Er, Yb, Lu) after steam exposure at 1400°C and 125 h for (A) stagnant steam velocity region showing the initial formation of RE_2SiO_5 (brighter phase), (B) intermediate steam velocity region where porous RE_2SiO_5 is the stable product phase (80–115 m/s), and (C) high-velocity steam region where RE_2O_3 is the stable product phase (165–185 m/s)

The impingement site, stagnant velocity region under the platinum foil sample holder, and the high-velocity regions of the sample are shown in backscattered electron images in Figure 11. The impingement site showed extensive material loss and a large through-crack that extended completely through the coupon. Under the platinum foil, the hexagonal structure $Nd_{9.33}\square_{0.67}Si_6O_{26}$ phase was present as a dense and heavily faceted reaction layer. All high-velocity regions (80–190 m/s) exhibit a porous $Nd_{9.33}\square_{0.67}Si_6O_{26}$ product phase where the grains are interconnected, analogous to faceting planes viewed in Figure 11B.

Cross-section analysis of $Nd_2Si_2O_7$ after steam exposure is shown in Figure 12. An excessively large porosity network is readily visible for both velocity regions displayed. Similar to $RE_2Si_2O_7$ (RE = Er, Yb, Lu), densification of the top-layer of the $Nd_{9.33}\square_{0.67}Si_6O_{26}$ product phase was seen when gas velocities are 150–190 m/s that resulted in a slightly decreased total reaction thickness, compared to intermediate velocities of 80–115 m/s. Figure 12C shows the EDS of the densified region in Figure 12B, where some peaks correlate to the carbon epoxy and Au/Pd conductive sample coating. EDS identification confirmed an Nd/Si atomic % ratio of 1.56, which agrees with the Nd/Si ratio for the $Nd_{9.33}\square_{0.67}Si_6O_{26}$ pattern determined by XRD. No other significant Nd/Si ratios were determined by EDS in either plan view or cross-section across the $Nd_2Si_2O_7$ coupon, further affirming that $Nd_{9.33}\square_{0.67}Si_6O_{26}$ is the only product phase forming upon steam reaction. An accurate impingement erosion depth for $Nd_2Si_2O_7$ was not measurable due to a through-thickness crack at the highest velocity impingement site after steam exposure.

4 | ANALYSIS

All five disilicate materials in this study ($RE_2Si_2O_7$, RE = Sc, Nd, Er, Yb, Lu) displayed porosity increases from a chemical reaction with high-velocity steam. Steam reaction products were rare-earth-rich phases, consistent with silica volatility as a silicon hydroxide gas species. $RE_2Si_2O_7$ (RE = Er, Yb, Lu) and $Nd_2Si_2O_7$ displayed densification of

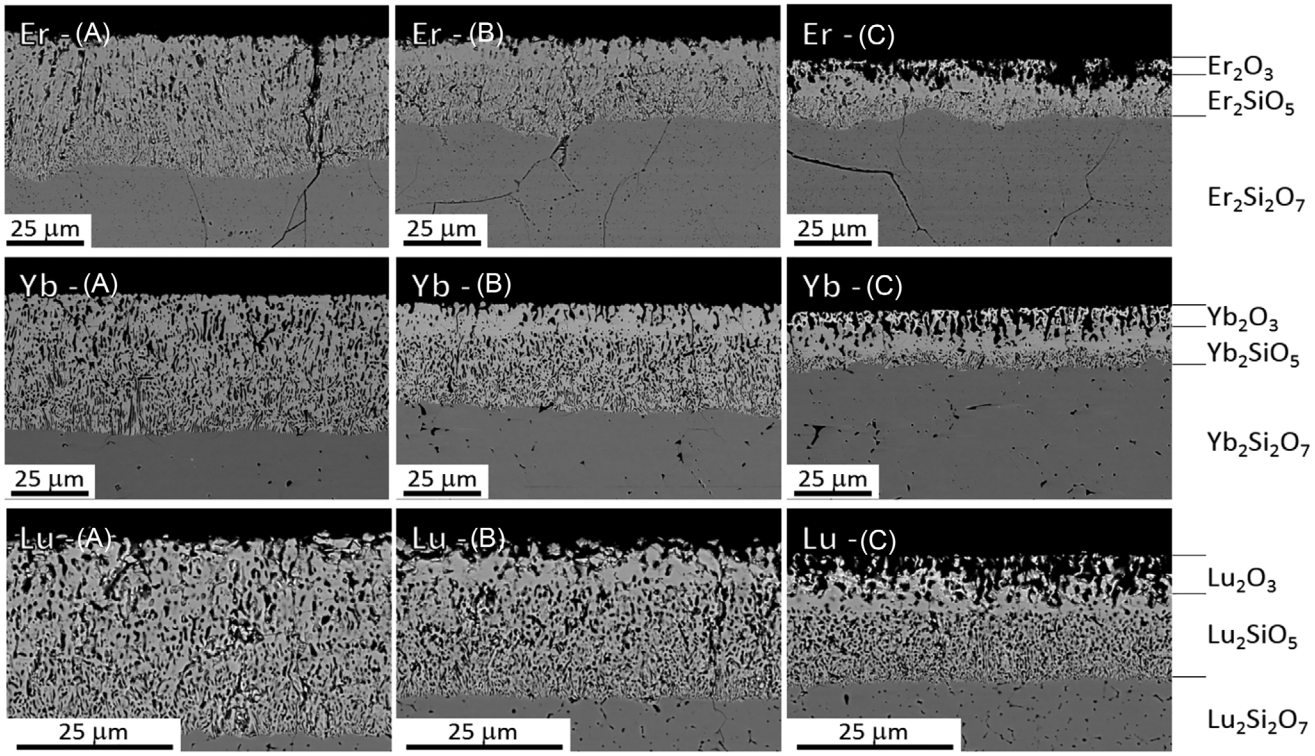

FIGURE 6 Cross-section SEM images of $RE_2Si_2O_7$ (RE = Er, Yb, Lu) after steam exposure at 1400°C and 125 h for steam velocity regions of (A) 80–115 m/s, (B) 120–140 m/s, and (C) 165–185 m/s. Lutetium silicate cross-section SEM images are provided at a higher magnification with a different scale bar

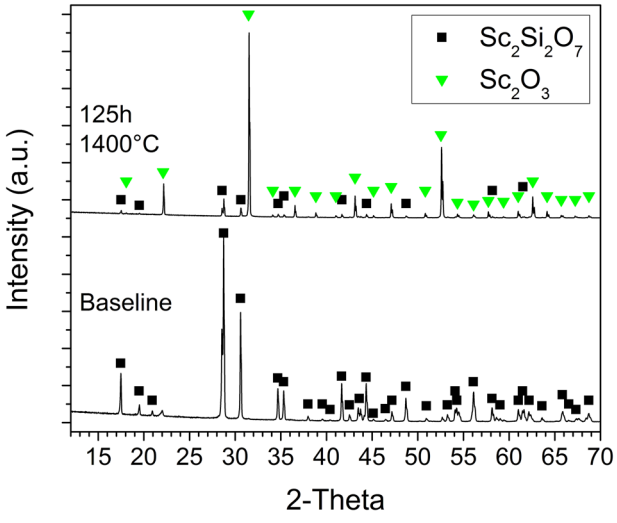

FIGURE 7 XRD of $Sc_2Si_2O_7$ baseline and after steam exposure at 1400°C for 125 h

the RE_2SiO_5 and $Nd_{9.33}\square_{0.67}Si_6O_{26}$ phases, respectively, where local gas velocities exceeded ~150 m/s. $Sc_2Si_2O_7$ uniquely did not form a silicate reaction product and did not show signs of microstructural evolution attributed to the high melting temperature of Sc_2O_3. The product phase morphologies for all samples displayed significantly less porosity in the stagnant gas velocity regions, indicating a change in the reaction process, compared to regions exposed to high-velocity steam.

A summation of the measured mass loss, average reaction depths for the steam velocity regions, and porosity production for the steam reaction products are presented in Table 4. It should be noted that mass loss data should be treated as qualitative since it includes mass uptake around the edges of the samples where the gas velocity is not high enough to inhibit contamination from the alumina tube furnace. Due to the lack of microstructural evolution and reaction depth changes for $Sc_2Si_2O_7$ (Figures 8C and 9A), the average reaction depth for $Sc_2Si_2O_7$ reaction represents the entire 80–200 m/s gas velocity range. The average reaction depth for the 80–115 m/s steam velocity range is analogous to the regions where a porous reaction product forms on the surface without microstructural evolution (Figures 5B, 6B, and 12A). The average reaction depth for the 150–200 m/s steam velocity range corresponds to both the densification of the reaction layer (RE = Nd, Er, Yb, Lu) and subsequent reaction to form a second outer product phase, such as rare-earth oxides for RE = Er, Yb, and Lu (Figures 5C, 6C, 11C). For each region, the average porosity area fraction is calculated to compare to theoretical volume changes for the expected steam reactions. The volatilization/erosion behavior at the highest velocity impingement site is recorded since the direct impingement

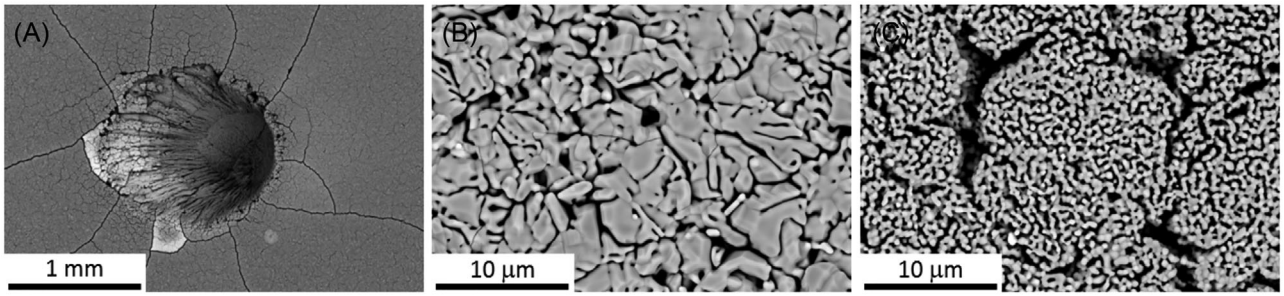

FIGURE 8 SEM images of $Sc_2Si_2O_7$ in plan view after steam exposure at 1400°C for 125 h, displaying (A) material mechanical erosion at the highest velocity impingement site (200–235 m/s), (B) Sc_2O_3 formation in the stagnant gas velocity region, and (C) Sc_2O_3 reaction product in the high steam velocity region (165–185 m/s)

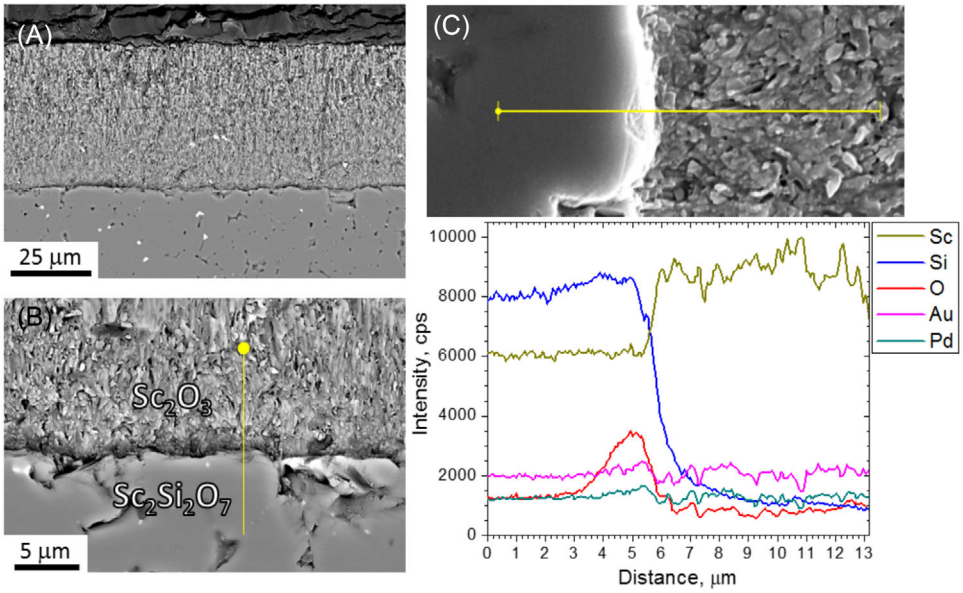

FIGURE 9 Cross-section SEM images of $Sc_2Si_2O_7$, after steam exposure at 1400°C for 125 h, displaying (A) Sc_2O_3 reaction product thickness at steam velocities 80–180 m/s, (B) $Sc_2Si_2O_7$-Sc_2O_3 reaction interface, and (C) EDS line scan across the reaction interface. A Au/Pd coating was applied to the sample surface to reduce charging in the SEM

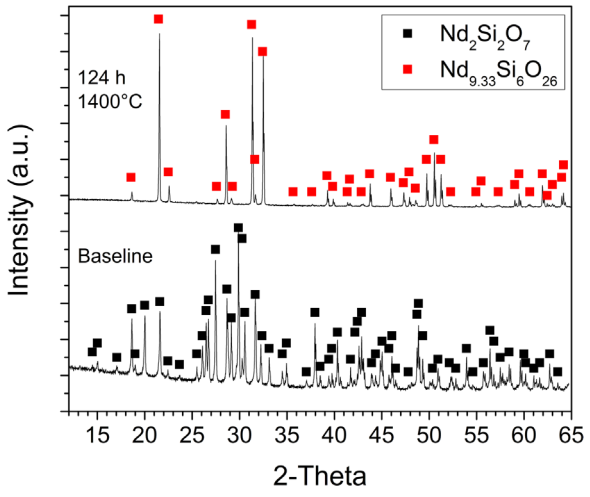

FIGURE 10 XRD of $Nd_2Si_2O_7$ baseline and after steam exposure at 1400°C for 124 h

of high-velocity steam can provide qualitative information on the resistance to mechanical erosion for each material.

Both $RE_2Si_2O_7$ (RE = Sc, Nd) exhibited larger amounts of mass loss than RE = Er, Yb, Lu). For $Sc_2Si_2O_7$, the cause of the mass loss is due to increased SiO_2 loss to directly form Sc_2O_3 instead of Sc_2SiO_5 formation. The formation of a fine Sc_2O_3 reaction product also resulted in decreased structural integrity at the highest velocity impingement site, resulting in a mechanical erosion depth of 241 ± 10 μm. $Nd_2Si_2O_7$ uniquely formed a reaction product $Nd_{9.33}\square_{0.67}Si_6O_{26}$, which has a higher SiO_2 concentration than a RE_2SiO_5 product phase. $Nd_2Si_2O_7$ showed the highest mass loss and largest average reaction depth of the disilicates in this study, reinforcing the concept that $Nd_2Si_2O_7$ is not desirable as a standalone EBC material.

$RE_2Si_2O_7$ (RE = Er, Yb, Lu) all displayed comparable steam reaction products, mass loss, average reaction

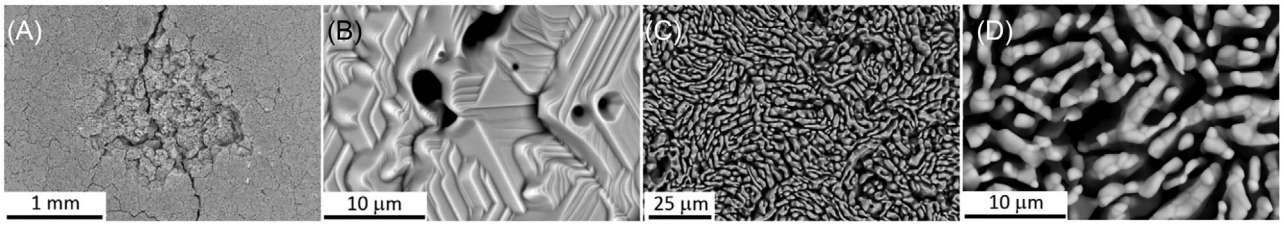

FIGURE 11 SEM images of $Nd_2Si_2O_7$ in plan view after steam exposure at 1400°C for 124 h, displaying (A) material mechanical erosion at the highest velocity impingement site (200–235 m/s), (B) hexagonal $Nd_{9.33}\square_{0.67}Si_6O_{26}$ formation in the stagnant gas velocity region, and (C/D) the $Nd_{9.33}\square_{0.67}Si_6O_{26}$ reaction product in the high steam velocity region (165–185 m/s)

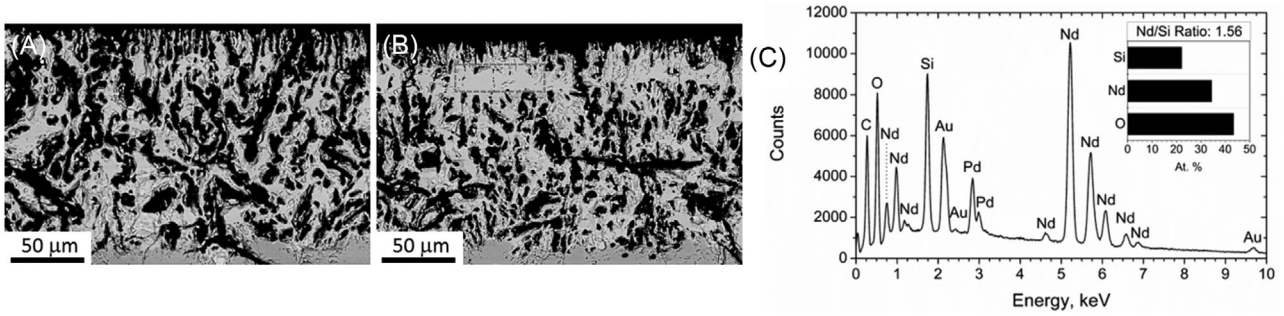

FIGURE 12 Cross-section SEM images of $Nd_2Si_2O_7$ after steam exposure at 1400°C for 125 h, displaying (A) $Nd_{9.33}\square_{0.67}Si_6O_{26}$ reaction product thickness at steam velocities 80–130 m/s, (B) $Nd_{9.33}\square_{0.67}Si_6O_{26}$ reaction product thickness at steam velocities 165–185 m/s, and (C) EDS of the reaction product zone marked by the box on Figure 12B

depths, porosity formation, and impingement erosion depths. Each coupon produced RE_2SiO_5 as the major product phase at gas velocities of 80–115 m/s. From 125–150 m/s, densification of the RE_2SiO_5 layer resulted in decreased total reaction thicknesses. RE_2O_3 was seen to form from the dense RE_2SiO_5 layer when gas velocities exceeded 150 m/s, which further decreased the total reaction depth. The theoretical volume difference between $Yb_2Si_2O_7$ and Yb_2SiO_5 is −24%, between Yb_2SiO_5 and Yb_2O_3 is −32%, and between $Yb_2Si_2O_7$ and Yb_2O_3 is −52%. Initial porosity in each material was subtracted from the porosity area fraction measured after steam exposure to give the porosity values presented in Table 4. Measured average porosity concentrations after steam exposure correlate well with the predicted volume changes. The thickness of the densified intermediate RE_2SiO_5 layer for Er was measurably denser than that of Yb and Lu, which resulted in decreased steam ingress to the reaction interface and thus a decreased total reaction depth in the 150–200 m/s steam velocity range. The cause of increased densification at higher velocities for $Er_2Si_2O_7$ is currently unknown, but may be a result of the lower melting temperature of $Er_2Si_2O_7$, compared to RE = Yb, Lu.

Using XRD and SEM/EDS analysis, the chemical reactions in Equations (4) and (5) for RE = Er, Yb, and Lu were confirmed, consistent with the literature. For RE = Sc and Nd (Equations 6 and 7), chemical reactions are proposed based on characterization of steam testing performed in this work. Theoretical volume changes are used for determining porosity production for the given reactions.

$$(\mathrm{RE} = \mathrm{Er},\ \mathrm{Yb},\ \mathrm{Lu})\ \mathrm{RE_2Si_2O_7} + 2\mathrm{H_2O\,(g)} \rightarrow \mathrm{RE_2SiO_5} + \mathrm{Si(OH)_4\,(g)} + 24\%\ \text{porosity}, \quad (4)$$

$$(\mathrm{RE} = \mathrm{Er},\ \mathrm{Yb},\ \mathrm{Lu})\ \mathrm{RE_2SiO_5} + 2\mathrm{H_2O\ (g)} \rightarrow \mathrm{RE_2O_3} + \mathrm{Si(OH)_4\,(g)} + 32\%\ \text{porosity}, \quad (5)$$

$$\mathrm{Sc_2Si_2O_7} + 4\mathrm{H_2O\,(g)} \rightarrow \mathrm{Sc_2O_3} + 2\mathrm{Si(OH)_4\,(g)} + 53\%\ \text{porosity}, \quad (6)$$

$$14\mathrm{Nd_2Si_2O_7} + 20\mathrm{H_2O\,(g)} \rightarrow 3\mathrm{Nd_{9.33}\square_{0.67}Si_6O_{26}} + 10\mathrm{Si(OH)_4\,(g)} + 15\%\ \text{porosity}. \quad (7)$$

The formation of Sc_2O_3 directly from $Sc_2Si_2O_7$ results in the increased H_2O (g) usage in the chemical reaction, compared to Equation (1) with a larger theoretical volume change of −53%. The chemical reaction for $Nd_2Si_2O_7$ is considered hypothetical due to the complexity

TABLE 4 Summary of measured mass loss, reaction depths, and area percent porosity produced for $RE_2Si_2O_7$ (RE = Sc, Nd, Er, Yb, and Lu) after high-velocity steam exposure at 1400°C for 125 h. *$Sc_2Si_2O_7$ reaction depth and produced porosity amount are average values over the entire 80–200 m/s steam velocity range

Sample	Mass loss (mg/cm^2)	Average reaction depth, 80–115 m/s (μm)	Porosity %, 80–125 m/s	Average reaction depth, 150–200 m/s (μm)	Porosity %, 150–200 m/s	Impingement depth, 200–235 m/s (μm)
$Sc_2Si_2O_7$	7.49	44 ± 2*	49%*	44 ± 2*	49%*	241 ± 10
$Nd_2Si_2O_7$	11.36	155 ± 5	47%	142 ± 7	47%	N/A
$Er_2Si_2O_7$	2.98	50 ± 3	29%	16 ± 3	36%	42 ± 7
$Yb_2Si_2O_7$	3.07	51 ± 2	23%	22 ± 3	43%	37 ± 6
$Lu_2Si_2O_7$	2.69	32 ± 2	24%	22 ± 3	39%	90 ± 4

of the reaction product. The theoretical porosity formation from $Nd_2Si_2O_7$ to $Nd_{9.33}\square_{0.67}Si_6O_{26}$ is −15%, which is much smaller than the measured porosity area fraction of −47%.

5 | DISCUSSION

$RE_2Si_2O_7$ (RE = Er, Yb, Lu) displayed comparable microstructural features across local regions of the sample surfaces. $Lu_2Si_2O_7$ showed the lowest specific mass loss and reaction depth for the 80–115 m/s steam velocity range, compared to RE = Er, Yb. At higher velocities, the Er_2SiO_5 product layer densified better than RE = Yb, Lu, which resulted in $Er_2Si_2O_7$ displaying smaller total reaction depths at steam velocities of 150–200 m/s. At the highest velocity impingement site, $Yb_2Si_2O_7$ displayed the smallest total reaction thickness with minimal mechanical erosion, while RE = Er and Lu did show mechanical erosion. Therefore, it is uncertain which parameter to use as a metric for EBC stability in steam. Future work should involve additional high-velocity steam testing to discern mechanisms for the microstructural evolution of $RE_2Si_2O_7$.

Klemm showed that the steam stability of bulk $Sc_2Si_2O_7$ was similar to bulk Sc_2SiO_5 after steam exposure in a burner rig at 1450°C for 100 h.[22] The results of the current study verify the lack of stability of Sc_2SiO_5 in steam environments and instead confirm that $Sc_2Si_2O_7$ reacts with steam to directly form Sc_2O_3 instead of the Sc_2SiO_5 phase. Unlike other $RE_2Si_2O_7$ in this work, the Sc_2O_3 product layer did not undergo densification in the 125–150 m/s steam velocity range as was seen for the RE_2SiO_5 (RE = Er, Yb, Lu) product phases. The stability of Sc_2O_3 as a product layer may result from an increased melting temperature of Sc_2O_3 (2472°C), compared to RE_2SiO_5 (1950–2000°C). It is likely that the Sc_2SiO_5 phase lacks high-temperature stability, compared to other rare-earth silicate phases. Alternatively, the increased steam reaction depth presented in Table 4 could occur due to both the $Sc_2Si_2O_7$-Sc_2SiO_5 and Sc_2SiO_5-Sc_2O_3 dual-phase fields having higher silica activities than the systems with RE = Er, Yb, or Lu. Thus, it cannot be assumed that $RE_2Si_2O_7$ of the same polymorph will have similar silica activities as was initially hypothesized. An increased silica activity for the scandium silicates may result from scandium's decreased mass and ionic radius, compared to the rare-earth cations in the lanthanide series. Additionally, extensive impingement site mechanical erosion was measured for the $Sc_2Si_2O_7$ sample. The erosion is presumably caused by the lack of structural integrity of the highly porous Sc_2O_3 product phase. Therefore, $Sc_2Si_2O_7$ is not recommended as a standalone EBC material.

$Nd_2Si_2O_7$ was exposed to steam for 124 h at 1400°C and formed a complex intermediate line compound, $Nd_{9.33}\square_{0.67}Si_6O_{26}$, as the steam reaction product. Figure 1 shows two low-melting eutectics for the SiO_2-$Nd_2Si_2O_7$ and Nd_2SiO_5-Nd_2O_3 phase fields, both of which are lower than those for the Sc- and Yb-silicate systems. Assuming rare-earth silicate melts have similar properties, the low-melting eutectics represent decreased stabilities of the $Nd_2Si_2O_7$ and Nd_2SiO_5 phases, compared to the other $RE_2Si_2O_7$ and RE_2SiO_5 (RE = Sc or Yb).

In addition, the Nd- apatite compound—presented on the phase diagram as $Nd_4Si_3O_{12}$ yet now commonly known as $Nd_{9.33}\square_{0.67}Si_6O_{26}$—has an increased stability relative to the Yb-apatite phase.[38] Thus, the phase diagram is consistent with experimental results of an Nd-apatite phase forming upon steam reaction. It is hypothesized that the silica activity of a $RE_2Si_2O_7$–$Nd_{9.33}\square_{0.67}Si_6O_{26}$ dual-phase field should be higher than a $RE_2Si_2O_7$–RE_2SiO_5 dual-phase field simply due to an increase in SiO_2 content for the apatite phase relative to the monosilicate phase. The increased steam reactivity of $Nd_2Si_2O_7$, compared to RE = Er, Yb, and Lu silicates also suggests that the A-polymorph $Nd_2Si_2O_7$–$Nd_{9.33}\square_{0.67}Si_6O_{26}$ phase field has a greater silica activity than the β-polymorph $RE_2Si_2O_7$ – RE_2SiO_5 (RE = Er, Yb, or Lu) phase fields. Single rare-earth cation $RE_2Si_2O_7$ EBC candidates should thus be limited to

rare-earth systems that do not have an increased stability of the rare-earth apatite phase, such as RE = Y, Ho, Er, Tm, Yb, or Lu.[13,38,39]

Excess mass loss and steam reactivity may be indicative of the lower melting temperature of $Nd_2Si_2O_7$, compared to other rare-earth silicates in this study. A lower melting temperature (higher homologous temperature) increases atom mobility and may encourage both higher steam reaction rates and rapid coarsening of the porous network. Alternatively, the apatite phase may be more prone to coarsening and texturing than the monosilicate phase, resulting in the coarse and aligned porosity channels observed within the apatite phase. Additionally, the total porosity production from the steam reaction far exceeded the predicted porosity uptake based on Equation 7. Slater et al. showed that oxide ion conductivity is high for the rare-earth apatite systems, and can be an order of magnitude higher along the c-axis of the apatite unit cell, compared to the a- and b-axes.[37] After steam exposure, the sample displayed preferential surface orientations of the (n00) hkl planes, n = 1-6, from XRD analysis, which are oriented parallel to the c-axis discussed by Slater et al. Increased mobility of oxygen and vacancies parallel to the sample surface may be contributing to the increased porosity concentration and coarsening of the porosity network in the apatite reaction product layer. The steam reaction for rare-earth disilicates that form an apatite reaction product should be studied further in future research.

The high-velocity steam stability of single rare-earth cation $RE_2Si_2O_7$ compounds is not universal. Thus, it is possible that multi- rare-earth silicate mixtures could promote certain steam reaction products, enhance structural integrity to limit high-velocity mechanical erosion, and tailor the steam reactivity for an optimized EBC material candidate. Further work should involve both a thermodynamic analysis of the rare-earth silicate compounds and high-velocity steam testing of other $RE_2Si_2O_7$ to develop trends in steam resistance and steam reaction products with varied rare-earth cations.

6 | CONCLUSION

The reactivity of five $RE_2Si_2O_7$ (RE = Sc, Nd, Er, Yb, Lu) EBC candidates was compared after exposure to high-velocity H_2O (g) at 1400°C for 125 h. $RE_2Si_2O_7$ for RE = Er, Yb, and Lu underwent a primary reaction to form a porous silica-depleted RE_2SiO_5, similar to prior results in the literature. The RE_2SiO_5 further reacted with H_2O (g) to form porous RE_2O_3. RE = Sc and Nd both showed unique steam reactions, where $Sc_2Si_2O_7$ formed only a Sc_2O_3 layer and $Nd_2Si_2O_7$ readily formed $Nd_{9.33}\square_{0.67}Si_6O_{26}$. This work demonstrates that rare earth disilicates do not all undergo the same behavior in high-velocity steam. Rare-earth cation considerations are thus important to consider for single rare-earth cation EBC coatings as well as multi-component EBC candidate materials.

ACKNOWLEDGMENTS

This research was supported by the National Science Foundation DMREF: Collaborative Research: GOALI: Accelerating Discovery of High Entropy Silicates for Extreme Environments, Award #1921973. The authors would like to acknowledge Dr. Bryan Harder (NASA, Glenn Research Center) for supplying the $Sc_2Si_2O_7$ and $Nd_2Si_2O_7$ powders, and the Nanoscale Materials Characterization Facility (NMCF) at the University of Virginia for supporting this research through characterization equipment.

ORCID

Mackenzie Ridley https://orcid.org/0000-0002-4043-2209

Elizabeth Opila https://orcid.org/0000-0001-5540-7084

REFERENCES

1. Opila EJ, Hann RE. Paralinear oxidation of CVD SiC in water vapor. J Am Ceram Soc. 1997;80(1):197–205. https://doi.org/10.1111/j.1151-2916.1997.tb02810.x
2. Gustavo C, Jacobson NS. Mass spectrometric measurements of the silica activity in the Yb_2O_3–SiO_2 system and implications to assess the degradation of silicate-based coatings in combustion environments. J Eur Ceram Soc. 2015;35:4259–67.
3. Jacobson N. Silica activity measurements in the Y_2O_3-SiO_2 system and applications to modeling of coating volatility. J Am Ceram Soc. 2014;97(6):1959–65.
4. Kowalski BA, Jacobson NS, Bodenschatz C, Costa G. Thermodynamics of the Lu_2O_3–SiO_2 system and comparison to other rare earth silicates. J Chem Thermodyn. 2021;161:106483. https://doi.org/10.1016/j.jct.2021.106483
5. Felsche J. *The crystal chemistry of the rare earth silicates, rare earths*. Berlin, Heidelberg: Springer; 1973.
6. Fernández-Carrión AJ, Allix M, Becerro AI. Thermal expansion of rare-earth pyrosilicates. J Am Ceram Soc. 2013;96(7):2298–305. https://doi.org/10.1111/jace.12388
7. Turcer LR, Padture NP. Towards multifunctional thermal environmental barrier coatings (TEBCs) based on rare-earth pyrosilicate solid-solution ceramics. Scr Mater. 2018;154:111–7. https://doi.org/10.1016/j.scriptamat.2018.05.032
8. Olesinski RW, Abbaschian GJ. The C–Si (Carbon-Silicon) system. Bull Alloy Phase Diagr. 1984;(5):486–9.
9. Dong Y, Ren K, Lu Y, Wang Q, Liu J, Wang Y. High-entropy environmental barrier coating for the ceramic matrix composites. J Eur Ceram Soc. 2019;39(7):2574–9. https://doi.org/10.1016/j.jeurceramsoc.2019.02.022
10. Sun L, Luo Y, Tian Z, Du T, Ren X, Li J et al. High temperature corrosion of $(Er_{0.25}Tm_{0.25}Yb_{0.25}Lu_{0.25})_2Si_2O_7$ environmental barrier coating material subjected to water vapor and molten calcium–magnesium–aluminosilicate (CMAS). Corros Sci. 2020;175:108881. https://doi.org/10.1016/j.corsci.2020.108881

11. Toropov NA, Bondar IA. High-temperature solid solutions of silicates of the rare earth elements. In: Lindgren E, editor. Transactions of the 8th International Ceramic Congress: May 14-19, 1962; Copenhagen: Association Europeenne De Ceramique; 1962. p. 85–103.
12. Toropov NA, Vasil'eva VA. Phase diagram of the binary system of scandium oxide and silica. Zh Neorg Khim. 1962;7(8):1938–45.
13. Toropov NA. Some rare earth silicates. Transactions of the 7th International Ceramic Congress; 1960 May 23-28; London, UK. Stoke-on-Trent, England: British Ceramic Society; 1960. p. 435–42.
14. Toropov NA, Kougiya MV. Phase ratios in the Nd_2O_3-SiO_2 system. Izvestiya Akademii Nauk SSSR, Neorganicheskie Materialy. 1971;7(7):1220–23.
15. Felsche J. Rare earth silicates with the apatite structure. J Solid State Chem. 1972;5:266–75. https://doi.org/10.1016/0022-4596(72)90039-4
16. Saal J, Dongwon S, Stevenson A, Messing G, Liu Z-K. First-principles thermochemistry and thermodynamic modeling of the Al2O3–Nd2O3–SiO2–Y2O3 pseudoquaternary system. J Am Ceram Soc. 2010;93(11):4158–67.
17. Hoai Le T, Tang K, Arnout S, Malfliet A, Blanpain B, Guo M. Thermodynamic assessment of the Nd_2O_3-CaO-SiO_2 ternary system. Calphad. 2016;55:157–64. https://doi.org/10.1016/j.calphad.2016.08.006
18. Toropov NA, Galakhov FY, Konovalova SF. Silicates of the rare earth elements communication 5. phase diagrams of the Dy2O3-SiO2 and Er2O3-SiO2 systems Bull Acad Sci USSR, Div Chem Sci. 1961;8:1271–7.
19. Ye X, Luo Y, Liu S, Wu D, Hou D, Yang F. Experimental study and thermodynamic calculation of Lu_2O_3-SiO_2 binary system. J Rare Earths. 2017;35(9):927–33. https://doi.org/10.1016/S1002-0721(17)60996-7
20. Lee KN, Fox DS, Bansal NP. Rare earth silicate environmental barrier coatings for SiC/SiC composites and Si_3N_4 ceramics. J Eur Ceram Soc. 2005;25(10):1705–15. https://doi.org/10.1016/j.jeurceramsoc.2004.12.013
21. Richards BT, Young KA, de Francqueville F, Sehr S, Begley MR, Wadley HNG. Response of ytterbium disilicate–silicon environmental barrier coatings to thermal cycling in water vapor. Acta Mater. 2016;106(Supplement C):1–14. https://doi.org/10.1016/j.actamat.2015.12.053
22. Klemm H. Silicon nitride for high-temperature applications. J Am Ceram Soc. 2010;93(6):1501–22. https://doi.org/10.1111/j.1551-2916.2010.03839.x
23. Ridley M, Opila E. Thermochemical stability and microstructural evolution of $Yb_2Si_2O_7$ in high-velocity high-temperature water vapor. J Eur Ceram Soc. 2020;41(5):3141–9. https://doi.org/10.1016/j.jeurceramsoc.2020.05.071
24. Ueno S, Jayaseelan DD, Ohji T, Lin H-T. Recession mechanism of $Lu_2Si_2O_7$ phase in high speed steam jet environment at high temperatures. Ceramics International. 2006;32(7):775–778. https://doi.org/10.1016/j.ceramint.2005.05.014
25. Maier N, Nickel KG, Rixecker G. High temperature water vapour corrosion of rare earth disilicates $(Y,Yb,Lu)_2Si_2O_7$ in the presence of $Al(OH)_3$ impurities. J Eur Ceram Soc. 2007;27(7):2705–13. https://doi.org/10.1016/j.jeurceramsoc.2006.09.013
26. Ueno S, Jayaseelan DD, Ohji T. Water vapor corrosion behavior of lutetium silicates at high temperature. Ceram Int. 2006;32(4):451–5. https://doi.org/10.1016/j.ceramint.2005.03.022
27. dos Santos e Lucato SL, Sudre OH, Marshall DB. A method for assessing reactions of water vapor with materials in high-speed, high-temperature flow. J Am Ceram Soc. 2011;94:s186–95. https://doi.org/10.1111/j.1551-2916.2011.04556.x
28. Golden RA, Opila EJ. A method for assessing the volatility of oxides in high-temperature high-velocity water vapor. J Eur Ceram Soc. 2016;36(5):1135–47. https://doi.org/10.1016/j.jeurceramsoc.2015.11.016
29. Parker CG, Opila EJ. Stability of the Y_2O_3-SiO_2 system in high-temperature, high-velocity water vapor. J Am Ceram Soc. 2020;103(4):2715–26. https://doi.org/10.1111/jace.16915
30. Smolin YI, Shepelev YF, Titov AP. Refinement of crystal-structure of thortveitite $Sc_2Si_2O_7$. Kristallografiya. 1972;17(4).857–58.
31. Chi LS, Chen HY, Deng SQ, Zhuang HH, Huang JS. Synthesis and crystal structure of $Nd_2Si_2O_7$ in low temperature form. J Struct Chem China. 1997;16:177–80.
32. Christensen AN. Investigation by the use of profile refinement of neutron powder diffraction data of the geometry of the $[Si_2O_7]6-$ ions in the high temperature phases of rare earth disilicates prepared from the melt in crucible-free synthesis. Zeitschrift für Kristallographie–Crystalline Materials. 1994;209(1):7–13. https://doi.org/10.1524/zkri.1994.209.1.7
33. Smolin YI, Shepelev YF, Butikova IK. Crystal structure of ytterbium pyrosilicate, Yb2Si2O7. J Struct Chem. 1971;12(2):248–52. https://doi.org/10.1007/BF00739109
34. Soetebier F, Urland W. Crystal structure of lutetium disilicate, Lu2Si2O7. Zeitschrift für Kristallographie–New Crystal Structures. 2002;217(1):22. https://doi.org/10.1524/ncrs.2002.217.1.22
35. Kobayashi K, Sakka Y. Rudimental research progress of rare-earth silicate oxyapatites: their identification as a new compound until discovery of their oxygen ion conductivity. J Ceram Soc Japan. 2014;122(1428):649–63. https://doi.org/10.2109/jcersj2.122.649
36. Masubuchi Y, Higuchi M, Kodaira K. Reinvestigation of phase relations around the oxyapatite phase in the Nd_2O_3–SiO_2 system. J Cryst Growth. 2003;247(1):207–12. https://doi.org/10.1016/S0022-0248(02)01908-5
37. Slater PR, Sansom JEH, Tolchard JR. Development of apatite-type oxide ion conductors. Chem Record. 2004;4(6):373–84. https://doi.org/10.1002/tcr.20028
38. Risbud AS, Helean KB, Wilding MC, Lu P, Navrotsky A. Enthalpies of formation of lanthanide oxyapatite phases. J Mater Res. 2001;16(10):2780–3. https://doi.org/10.1557/JMR.2001.0381
39. Costa G, Harder BJ, Bansal NP, Kowalski BA, Stokes JL. Thermochemistry of calcium rare-earth silicate oxyapatites. J Am Ceram Soc. 2020;103(2):1446–53. https://doi.org/10.1111/jace.16816

How to cite this article: Ridley M, Opila E. Variable thermochemical stability of $RE_2Si_2O_7$ (RE = Sc, Nd, Er, Yb, or Lu) in high-temperature high-velocity steam. J Am Ceram Soc. 2021;1–13. https://doi.org/10.1111/jace.18120